

Diffusion-Based sRGB Real Noise Generation via Prompt-Driven Noise Representation Learning

Jaekyun Ko^{1*} Dongjin Kim^{2*} Soomin Lee² Guanghui Wang³ Tae Hyun Kim^{2†}

¹Mobile Experience Division, Samsung Electronics

²Department of Computer Science, Hanyang University

³Department of Computer Science, Toronto Metropolitan University

jkko1124.ko@samsung.com {dongjinkim,min001017,taehyunkim}@hanyang.ac.kr wangcs@torontomu.ca

Abstract

*Denoising in the sRGB image space is challenging due to noise variability. Although end-to-end methods perform well, their effectiveness in real-world scenarios is limited by the scarcity of real noisy-clean image pairs, which are expensive and difficult to collect. To address this limitation, several generative methods have been developed to synthesize realistic noisy images from limited data. These generative approaches often rely on camera metadata during both training and testing to synthesize real-world noise. However, the lack of metadata or inconsistencies between devices restricts their usability. Therefore, we propose a novel framework called **Prompt-Driven Noise Generation (PNG)**. This model is capable of acquiring high-dimensional prompt features that capture the characteristics of real-world input noise and creating a variety of realistic noisy images consistent with the distribution of the input noise. By eliminating the dependency on explicit camera metadata, our approach significantly enhances the generalizability and applicability of noise synthesis. Comprehensive experiments reveal that our model effectively produces realistic noisy images and show the successful application of these generated images in removing real-world noise across various benchmark datasets.*

1. Introduction

Real-world denoising is particularly challenging in low-level vision tasks due to the inherent complexity and diversity of real noise. Unlike additive white Gaussian noise (AWGN), which can be effectively modeled under controlled laboratory conditions, real-world noise arises from various sources such as sensor imperfections, lighting variations, in-camera processing pipelines, and adjustable camera settings. Consequently, real-world noise frequently exhibits signal-dependent and spatially varying properties.

A common solution to this issue is to construct extensive paired datasets consisting of noisy-clean image pairs and subsequently train end-to-end denoising networks in a supervised manner [6, 7, 21, 69, 70]. However, collecting such datasets is both resource-intensive and technically demanding [1, 3, 36, 41, 65]. To avoid this bottleneck, recent approaches generate synthetic real-world noise using metadata which includes sensor information such as camera manufacturer, ISO settings, shutter speed, and other parameters [2, 20, 22, 26, 38, 68]. This metadata serves as a compact representation of how an image signal processor (ISP) transforms a RAW to an sRGB image, thereby enabling an accurate simulation of the noise characteristics.

Despite their effectiveness, metadata-driven approaches [2, 11, 20, 26] encounter practical limitations. As illustrated in Fig. 1 (a), publicly available sRGB images on the website often lack original EXIF tags due to post-processing, resulting in metadata being unavailable. In domains like scientific imaging, metadata semantics and formats vary greatly or may be absent, making standard metadata methods ineffective. Therefore, approaches relying on specific metadata formats struggle to generalize well across diverse real-world scenarios.

Hence, in this work, we propose **Prompt-Driven Noise Generation (PNG)** model, a novel framework that eliminates the dependency on explicit metadata during both training and noise generation stages. As illustrated in Fig. 1(b), we propose a noise representation strategy utilizing prompt features, capturing input-specific noise characteristics directly from input noise images. These prompt features are generated via learnable prompt components, serving as a comprehensive repository of noise distributions. By conditioning the model on these learned prompt features, our framework enables a unified noise generator capable of synthesizing realistic noise. This design alleviates the dependency on metadata, which is often inconsistent, non-standard, or unavailable in both training and inference phases.

*Equal contribution.

†Corresponding author.

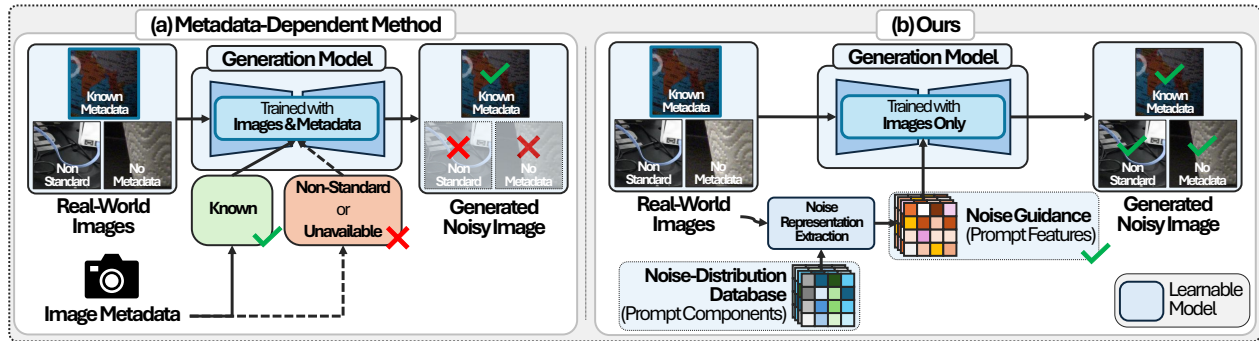


Figure 1. Noise Generation Comparison. (a) Metadata-dependent approach. (b) Ours.

Specifically, we introduce a **Prompt AutoEncoder (PAE)** that encodes the noise of the input image and produces input-specific prompt features including the characteristics of the input noise, such as ISO levels (gain) and noise correlation patterns. We then use a consistency model (CM) [35, 54], a diffusion-based generative model, to learn the latent space of the PAE and synthesize a new latent code conditioned on the extracted high-dimensional prompt features, which encapsulate information about the noise characteristics. Precisely, building on recent diffusion transformer (DiT) [39] architectures based on CM, we present a **Prompt DiT (P-DiT)** that fully leverages the prompt features from the PAE during the generation process. Finally, the Decoder of our PAE takes the synthesized latent code from P-DiT together with the clean image, and produces a noisy image, thereby simulating signal-dependent noisy image. Through extensive experiments, we demonstrate that our PNG achieves outstanding real-world noise modeling quality without requiring any metadata during the training or testing phases. For downstream tasks, we trained conventional supervised image denoising networks on the generated noisy dataset, achieving state-of-the-art (SOTA) real-world denoising performance across diverse domains, including smartphones, and DSLR cameras.

2. Related Works

sRGB Noise Generation. The limited availability of real-world noise datasets results in overfitting issues for denoising networks, particularly in practical applications [2, 8, 16, 27, 37, 59, 60, 68, 71, 75]. To tackle this problem, various methods for generating sRGB noise have been proposed. Flow-sRGB [26] leverages normalizing flows to model noise distributions based on factors like smartphone type and gain settings. NeCA [11] introduces a neighboring correlation-aware noise model for synthesizing realistic noise, explicitly accounting for both signal dependency and neighboring noise correlations. However, these methods depend on explicit metadata for noise generation, limiting their applicability in situations where such information is unavailable. To address this, NAFlow [20] introduces a noise-aware sampling algo-

rithm to synthesize sRGB noise without requiring metadata during inference. However, it still requires metadata during the training phase. In contrast to these previous approaches, our approach offers a metadata-free noise generation method for both training and testing phases by leveraging prompt features as noise guidance that capture input-noise-specific information.

Prompt Learning. In natural language processing, prompts (brief textual snippets) are prepended or appended to input sequences to guide large language models (LLMs) toward specific behaviors or outputs [4, 46, 48]. These prompts offer an auxiliary context, effectively transforming downstream tasks into instances that closely resemble the original pre-training objectives of the model.

Recently, this concept has been extended into computer vision by substituting fixed textual prompts with learnable prompts, either embedded into the input sequences or intermediate layers. The lightweight prompt parameters allow models to efficiently adapt to new domains or tasks [28–30, 42, 56, 57, 63, 73, 74]. For example, PromptIR [42], an all-in-one low-level image restoration framework, introduces a compact set of learnable prompts that dynamically interact with degradation features, providing specific degradation guidance and efficiently adapting the model to various restoration tasks.

Inspired by these works, we conceptualize prompts as compact representations of real-world noise characteristics. Our proposed PAE extracts high-dimensional prompt features that capture detailed sensor-specific statistics such as ISO levels, spatial correlations, and other noise attributes. Subsequently, our P-DiT leverages these prompt features to conditionally generate realistic sRGB noise. Thus, our method replaces explicit metadata with prompt-based representations, enabling precise control and substantially improving both the realism and diversity of the synthesized noisy images.

3. Proposed Method

3.1. Preliminaries

Diffusion Models. Diffusion models [13, 31, 49, 51, 61, 62, 64] involve a forward process that corrupts the data with independent and identically distributed Gaussian noise, followed by a learning phase to reverse this corruption. In the forward process, Gaussian random noise is added to the given input \mathbf{x}_0 . Using reparameterization, this process at timestep t can be represented as:

$$\mathbf{x}_t = \alpha_t \mathbf{x}_0 + \sigma_t \boldsymbol{\epsilon}, \quad \boldsymbol{\epsilon} \sim \mathcal{N}(0, \mathbf{I}), \quad t \in \{0, 1, \dots, T\} \quad (1)$$

where \mathbf{x}_t is the noise-added data sample at timestep t , \mathbf{I} denotes the identity matrix, σ_t is a noise schedule that controls the level of noise (*e.g.*, standard deviation of Gaussian noise), and α_t is a time-dependent function that defines the specific type of diffusion process, such as the variance-preserving [13, 49] and variance-exploding (VE) [51, 53] diffusion processes [23]. In this work, we employ the VE diffusion process, where $\alpha_t=1$. The objective of diffusion models is to reverse the forward process by denoising the corrupted sample \mathbf{x}_t back to the original data \mathbf{x}_0 .

In the context of score-based generative models [51–53], the score model $s_\theta(\mathbf{x}_t, \sigma_t)$ estimates the score function, a vector field that points toward regions of higher data density, by employing score matching [14, 53]. The reverse process is performed by iteratively applying the learned score function to gradually denoise the noisy input. This can be represented using probability flow ordinary differential equations (PF ODEs), as described in [18] as:

$$d\mathbf{x}_t = -\dot{\sigma}_t \sigma_t \nabla_{\mathbf{x}_t} \log p(\mathbf{x}_t; \sigma_t) dt, \quad (2)$$

where the score function is $\nabla_{\mathbf{x}_t} \log p(\mathbf{x}_t; \sigma_t)$. In practice, solving this reverse-time ODE involves numerous update steps, which makes diffusion models computationally intensive.

Consistency Models. Unlike traditional diffusion models that generate data through multiple iterative steps, recent consistency models (CMs) streamline the process by achieving results in a single step [50, 54]. Specifically, the CM learns a mapping function $f_\theta(\mathbf{x}_t, \sigma_t)$ such that, for any \mathbf{x}_t , the output remains *consistent* with the original data \mathbf{x}_0 . This process can be approximated as follows:

$$f_\theta(\mathbf{x}_t, \sigma_t) = \mathbf{x}_t + \int_{\sigma_t}^{\sigma_0} \frac{d\mathbf{x}_u}{du} du \approx \mathbf{x}_0. \quad (3)$$

The consistency training (CT) loss ensures that the model’s outputs remain stable across different noise levels, as follows:

$$\mathcal{L}_{CT} = \mathbb{E}[\lambda(\sigma_t) d(f_\theta(\mathbf{x}_{t+1}, \sigma_{t+1}) - \text{sg}(f_{\theta^-}(\mathbf{x}_t, \sigma_t)))], \quad (4)$$

where $\lambda(\cdot)$ is a weighting function, $d(\cdot)$ is a distance function like pseudo-Huber loss [50], and $\text{sg}(\cdot)$ denotes the stop-gradient operator. Here, f_θ and f_{θ^-} refer to the student and teacher networks, respectively. The stop-gradient operator is used to keep the teacher network fixed during each optimization step of the student network. In our approach, since the pretrained teacher model is not available, we set $\theta^- = \theta$ as in [25, 50, 54]. We adopt most of the training hyperparameters for the CM from EDM [18] and iCT [50], and further details are in Sec. S.2.

3.2. Overall Flow: PNG

We introduce a novel Prompt-Driven Noise representation framework (PNG), designed to generate realistic noisy images by substituting explicit metadata (*e.g.*, smartphone manufacturer, ISO settings) with learned prompt components. Inspired by recent latent diffusion models [35, 43], PNG operates within a compact latent space, achieving significant computational efficiency via CM. This approach notably reduces computational overhead compared to methods operating directly in image space. The overall flow of PNG is depicted in Fig. 2, comprising two primary components: the Prompt Autoencoder (PAE) and the Prompt DiT (P-DiT), trained sequentially in a two-stage process.

Two-Stage Training Phase. First, we train a U-Net-based [45] PAE to learn a compact latent representation. As illustrated in Fig. 2 (a), the PAE consists of a Prompt Encoder \mathcal{E} and a Decoder \mathcal{D} . The Prompt Encoder \mathcal{E} maps the input noise \mathbf{n}_{Real} representing the residual between the paired noisy image $\mathcal{I}_{\text{Noisy}}$ and the clean image $\mathcal{I}_{\text{Clean}}$ (*i.e.* $\mathbf{n}_{\text{Real}} = \mathcal{I}_{\text{Noisy}} - \mathcal{I}_{\text{Clean}}$) into a latent code \mathbf{z} . Moreover, the Prompt Encoder learns global and local prompt components, $\mathbf{P}_{\text{Global}}$ and $\mathbf{P}_{\text{Local}}$, as learnable parameters that encode real world noise characteristics from the training set and are optimized jointly with the PAE. Given the clean image $\mathcal{I}_{\text{Clean}}$, the Decoder \mathcal{D} reconstructs the noisy image $\tilde{\mathcal{I}}_{\text{Noisy}}$ from the latent code \mathbf{z} , learning signal-dependent characteristics simultaneously.

Subsequently, the P-DiT is trained to model the latent code distribution of the PAE using a CM-based objective \mathcal{L}_{CT} in Eq. (4). Given the fully trained Prompt Encoder \mathcal{E} , the P-DiT learns to synthesize latent codes embedding input-specific noise characteristics, leveraging encoded latent code \mathbf{z}_0 , prompt features $\mathbf{F}_{\text{Global}}$ and $\mathbf{F}_{\text{Local}}$ from \mathcal{E} , and the clean image $\mathcal{I}_{\text{Clean}}$.

Inference Phase. As illustrated in Fig. 2 (b), during the generation phase, the Prompt Encoder \mathcal{E} produces prompt features that capture the characteristics of input noise \mathbf{n}_{Real} . Specifically, the prompt features are dynamically generated by modulating the prompt components $\mathbf{P}_{\text{Global}}$ and $\mathbf{P}_{\text{Local}}$, conditioning on the input noise. Given the resulting prompt features and a clean image, P-DiT transforms a sampled latent variable \mathbf{z}_T (see Eq. (1)) into a latent code $\hat{\mathbf{z}}_0$. The

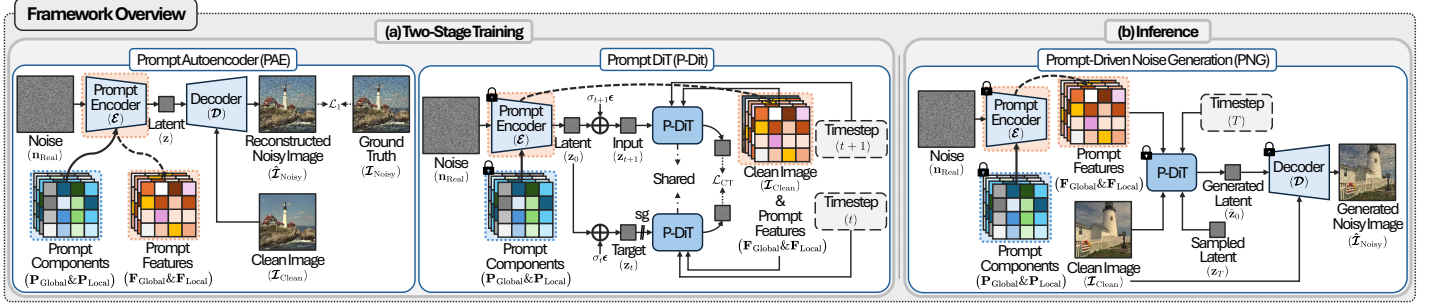


Figure 2. Overview of the proposed method. (a) Training pipeline. (b) Inference pipeline.

Decoder \mathcal{D} then converts \hat{z}_0 into the final noisy image $\hat{\mathcal{I}}_{\text{Noisy}}$, conditioned on the clean image $\mathcal{I}_{\text{Clean}}$.

3.3. Prompt Autoencoder

3.3.1. Prompt Encoder

As depicted in Fig. 3, the Prompt Encoder \mathcal{E} is composed of several convolutional layers, including residual blocks [12], and incorporates two key modules: the Global Prompt Block (GPB) and the Local Prompt Block (LPB). These modules dynamically generate prompt features by leveraging learnable prompt components guided by extracted real-world noise characteristics, such as ISO levels and noise correlation. The resulting prompt features are concatenated with the input features, embedding informative latent codes. Through training, the learnable prompt components within both GPB and LPB adaptively capture the underlying data distribution, allowing the prompt features to serve as implicit representations of input noise characteristics, thereby effectively replacing the need for explicit noise metadata.

Global Prompt Block. A camera ISP can adjust brightness using ISO (gain), simulating physical exposure. However, increasing the signal gain through high ISO settings also amplifies sensor noise. Thus, ISO is a crucial factor in modeling noise attributes. To capture global noise statistics, such as noise amplification in the prompt features, we propose the Global Prompt Block (GPB). This block is designed to analyze how different ISO levels impact noise characteristics, allowing our model to better represent the inherent noise patterns associated with varying ISO settings.

In the GPB, we first define a set of learnable global prompt components $\mathbf{P}_{\text{Global}}^\ell \in \mathbb{R}^{\frac{H}{2^\ell} \times \frac{W}{2^\ell} \times C_{\text{Global}}^\ell}$ to capture the global statistics at scale level $\ell \in \{0, 1, 2, 3\}$, where H , W , and C represent the height, width, and channel dimension of the corresponding feature maps, respectively. To generate the global prompt features $\mathbf{F}_{\text{Global}}^\ell \in \mathbb{R}^{\frac{H}{2^\ell} \times \frac{W}{2^\ell} \times C_{\text{Global}}^\ell}$, we compute input-specific coefficients $\mathbf{w}_{\text{Global}}^\ell \in \mathbb{R}^{1 \times 1 \times C_{\text{Global}}^\ell}$ from the input feature $\mathbf{F}_{\text{In}}^\ell \in \mathbb{R}^{\frac{H}{2^\ell} \times \frac{W}{2^\ell} \times C_{\text{In}}^\ell}$ by computing the channel-wise mean and standard deviation of the input feature to capture the global statistics of the input noise as:

$$\mathbf{w}_{\text{Global}}^\ell = \text{Softmax} \left(\text{Conv}_{1 \times 1} \left[\left[\mu(\mathbf{F}_{\text{In}}^\ell), \Sigma(\mathbf{F}_{\text{In}}^\ell) \right] \right] \right), \quad (5)$$

where $\mu(\cdot)$ and $\Sigma(\cdot)$ represent functions that compute the channel-wise mean and standard deviation, respectively. These two moments are concatenated and passed through a 1×1 convolutional layer, followed by a softmax operation. Then, these coefficients are adopted to dynamically modify the global prompt components $\mathbf{P}_{\text{Global}}^\ell$, followed by a 3×3 convolutional layer for refinement, to yield the final global prompt features $\mathbf{F}_{\text{Global}}^\ell$ as:

$$\mathbf{F}_{\text{Global}}^\ell = \text{Conv}_{3 \times 3} \left(\mathbf{w}_{\text{Global}}^\ell \odot \mathbf{P}_{\text{Global}}^\ell \right), \quad (6)$$

where \odot denotes the element-wise multiplication. This process ensures that the global prompt features reflect the global noise characteristics based on noise distribution statistics in the input image.

Local Prompt Block. In the GPB, we extract global information (e.g., ISO); however, real-world sRGB noise cannot be fully characterized by global information alone. This issue arises from several transformations in the ISP pipeline, such as non-linear and locally different spatial operations, which cause patterned, and non-*iid* noise during the RAW-to-sRGB conversion. Therefore, we additionally propose the Local Prompt Block (LPB) to capture camera model-specific noise characteristics from the input noise.

In the LPB, we first extract $\rho \times \rho$ patch from the input noise $\mathbf{n}_{\text{Real}} \in \mathbb{R}^{H \times W \times 3}$ at every pixel location and calculate the local correlation map for each patch with respect to its center pixel. Specifically, following the approach in LGBPN [59], we compute the Pearson correlation coefficients of neighboring pixels relative to the center pixel for each patch. This operation is applied to all patches, resulting in correlation coefficient maps $\mathbf{F}^\rho \in \mathbb{R}^{H \times W \times \rho^2}$, where each pixel contains its local correlation information along the channel axis. We then separately compute row-wise and column-wise averages from \mathbf{F}^ρ to capture local distortions introduced by the ISP pipeline within each patch. These two averages are then concatenated and upsampled using correlation map block (CoMB) which consists of lightweight operations, including a 1×1 convolutional layer, a bilinear upsampler, and a 3×3 convolutional layer, as illustrated in Fig. 3 (b). Similar to the GPB, we apply a softmax oper-

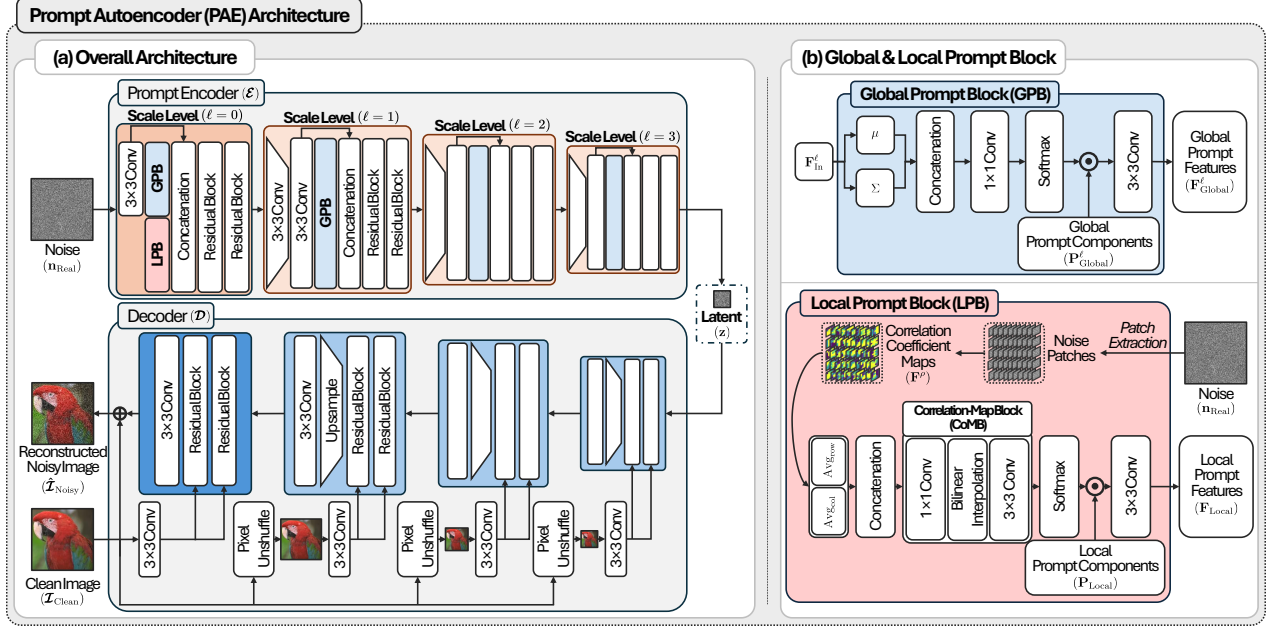


Figure 3. (a) Sketch of the Prompt Autoencoder (PAE). (b) Details of Global and Local Prompt Blocks.

ation to the upscaled features to generate the local prompt coefficients $\mathbf{w}_{\text{Local}} \in \mathbb{R}^{H \times W \times C_{\text{Local}}}$ defined as

$$\mathbf{w}_{\text{Local}} = \text{Softmax} \left(\text{CoMB} \left(\left[\text{Avg}_{\text{row}}(\mathbf{F}^{\rho}), \text{Avg}_{\text{col}}(\mathbf{F}^{\rho}) \right] \right) \right), \quad (7)$$

where Avg_{row} and Avg_{col} indicate row-wise and column-wise averaging operations, respectively. Next, the local prompt coefficients are multiplied element-wise by the prompt components $\mathbf{P}_{\text{Local}} \in \mathbb{R}^{H \times W \times C_{\text{Local}}}$ for dynamic feature aggregation, yielding the local prompt features $\mathbf{F}_{\text{Local}} \in \mathbb{R}^{H \times W \times C_{\text{Local}}}$ as follows:

$$\mathbf{F}_{\text{Local}} = \text{Conv}_{3 \times 3} \left(\mathbf{w}_{\text{Local}} \odot \mathbf{P}_{\text{Local}} \right). \quad (8)$$

We emphasize that by leveraging local noise characteristics (e.g., noise local correlation), the prompt components learn to focus on unique camera-specific features.

3.3.2. Decoder

As illustrated in the lower part of Fig. 3 (a), the Decoder \mathcal{D} consists of numerous convolutional layers, integrating residual blocks and upsampling operations to transform latent codes back into noisy images. The upsampling operation increases the spatial resolution of input features at scale ℓ using nearest-neighbor upsampling, as followed by [44]. To further capture the signal-dependent characteristics of real-world noise, clean images are downsampled using pixel downsampling [47], preserving fine-grained textures and conditioning at each scale level.

3.4. Prompt DiT (P-DiT)

We introduce P-DiT, which fully leverages the prompt features extracted from the Prompt Encoder \mathcal{E} to synthesize

latent codes $\hat{\mathbf{z}}_0$ that align with the embedded information of the input noise characteristics and the clean image provided. Our P-DiT is based on DiT [39], a transformer-based CM architecture specifically designed for training diffusion models. See Sec. S.1 in the supplementary material for detailed P-DiT architecture description.

4. Experiments

4.1. Experimental Setup

Implementation Details The PAE is trained with the Adam optimizer [24] and minimizes the \mathcal{L}_1 loss between the noisy image $\mathcal{I}_{\text{Noisy}}$ and the reconstructed noisy image $\hat{\mathcal{I}}_{\text{Noisy}}$, along with the \mathcal{L}_2 regularization applied to the latent code \mathbf{z} for dense representation [44]. We start with an initial learning rate $1e-4$, which is then reduced to $1e-6$ using a cosine annealing algorithm [33] over 400k iterations. We use randomly cropped patches of size 256×256 and a mini-batch size of 64 for training.

The P-DiT model is optimized with the RAdam optimizer [32] using a fixed learning rate of $2e-4$ over 250k iterations, applying the pseudo-Huber loss for Eq. (4), similar to iCT [50]. We also use randomly cropped patches of size 256×256 to embed latent codes of size 32×32 , with a mini-batch size of 512 during training. For the ablations, the mini-batch size is reduced to 128 to save training time. More details regarding the training process and model configurations are in Sec. S.2 and Sec. S.3, respectively.

For sRGB image denoising, we employ the DnCNN architecture [72], trained for 100k iterations with the Adam optimizer. All hyperparameters follow the setup in [11, 20], using a learning rate of $1e-3$, patch size of 96×96 , and a

Table 1. Quantitative results for synthetic noise on a subset of the SIDD validation set, in which the ISO values exist in the training set. The results are computed with KLD \downarrow and AKLD \downarrow . The best and second-best results are shown in **bold** and underline.

Camera	Metrics	C2N	Flow-sRGB	NeCA-W	NAFlow	Ours
G4	KLD	0.1660	0.0507	<u>0.0242</u>	0.0254	0.0174
	AKLD	0.2007	0.1504	0.1524	<u>0.1367</u>	0.1283
GP	KLD	0.1315	0.0781	0.0432	<u>0.0352</u>	0.0143
	AKLD	0.1968	0.1797	0.1273	<u>0.1180</u>	0.1074
IP	KLD	0.0581	0.5128	0.0410	<u>0.0339</u>	0.0291
	AKLD	0.2929	1.7490	<u>0.1145</u>	0.1522	0.1128
N6	KLD	0.3524	0.2026	<u>0.0206</u>	0.0309	0.0167
	AKLD	0.2919	0.2469	0.1304	<u>0.1108</u>	0.1106
S6	KLD	0.4517	0.3735	0.0302	<u>0.0272</u>	0.0193
	AKLD	0.4190	0.2641	0.1933	<u>0.1355</u>	0.1223
Average	KLD	0.2129	0.2435	0.0342	<u>0.0305</u>	0.0194
	AKLD	0.2802	0.5180	0.1436	<u>0.1306</u>	0.1163

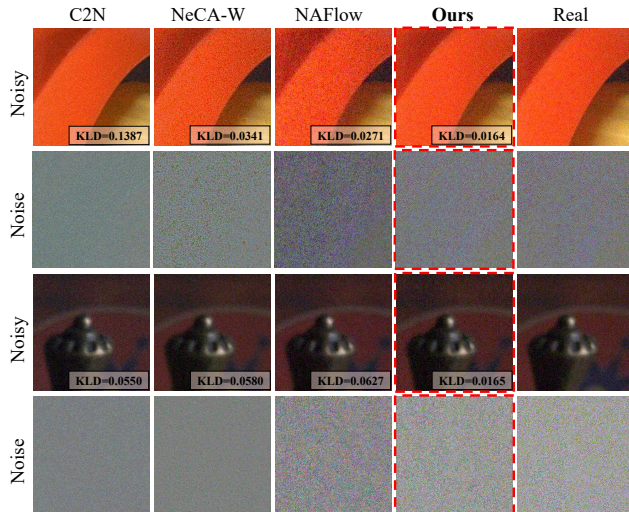


Figure 4. Visualization of synthetic noisy images on the SIDD validation set. From left to right: C2N, NeCA-W, NAFlow, Ours (PNG), and real noisy images.

mini-batch size of 8.

Metrics. To examine the quality of the generated noise, we use two metrics: Kullback-Leibler Divergence (KLD) and Average Kullback-Leibler Divergence (AKLD) [67]. In addition, we employ PSNR and SSIM metrics to assess the performance of the denoising.

4.2. Real-World sRGB Noise Generation and Removal

Dataset. We employ the SIDD [1] dataset, which includes 34 different camera configurations. We adopt the SIDD Medium split, comprising 320 noisy-clean image pairs captured with five unique smartphone cameras: Google Pixel (GP), iPhone 7 (IP), Samsung Galaxy S6 Edge (S6), Motorola Nexus 6 (N6), and LG G4 (G4). To evaluate the quality of the generated noise, we use the SIDD validation set. Additionally, the SIDD+[3], PolyU[65], and Nam [36] are employed to further assess both noise quality and denoising performance.

Table 2. Denoising performance of DnCNN on SIDD-Benchmark in terms of PSNR \uparrow and SSIM \uparrow . All methods are trained with synthetic noisy-clean pairs. Note that *Real* is trained with real noisy-clean pairs. The best and second-best results are highlighted in **bold** and underline.

Metrics	C2N	NoiseFlow	Flow-sRGB	NeCA-W	NAFlow	Ours	Real
PSNR \uparrow	33.76	33.81	34.74	36.82	<u>37.22</u>	37.55	37.63
SSIM \uparrow	0.901	0.894	0.912	0.932	<u>0.935</u>	0.937	0.936

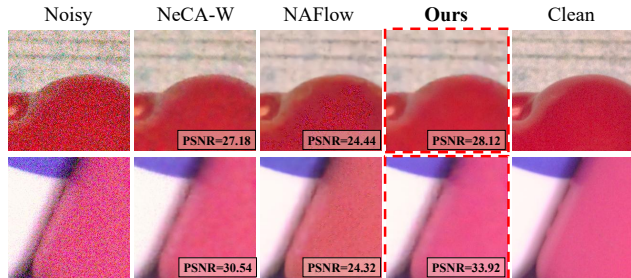


Figure 5. Visual comparison on denoising results with PSNR \uparrow on SIDD validation set from DnCNN trained on each method. For more qualitative results, please refer to the supplementary material.

Device-Specific Noise Quality Assessment. In Tab. 1, we train a single unified PNG on the full SIDD training set using all devices and evaluate the noise quality of each smartphone device type to assess device-specific noise generation performance in terms of KLD and AKLD. Our method is compared with four other models: C2N [16], Flow-sRGB [26], NeCA-W [11], and NAFlow [20]. Note that, to align with the experimental settings of previous works, we utilize some of the paired noisy-clean images from the SIDD validation set for noise generation, for images where the same metadata (e.g., smartphone manufacturer, ISO setting) is available for both the validation set and the training set.

In comparison, our PNG outperforms other methods across all device types, showing substantial improvements over NAFlow (the state-of-the-art at the time of submission) in both average KLD and AKLD scores, with improvements of 0.0111 and 0.0143, respectively. We also present visual comparisons of the noisy images generated by each method in Fig. 4. PNG generates more natural and realistic noise that closely resembles real-world noise distributions in magnitude and correlation patterns, demonstrating its superior performance in generating realistic noise.

Denoising Results on SIDD. To assess the accuracy of noise generation methods, we train DnCNN denoising networks using generated noisy-clean paired datasets from multiple domains, such as DSLR and smartphone, and compare their denoising performance. In Tab. 2, we compare the DnCNN denoising performance of our PNG with C2N, Flow-sRGB, NeCA-W, NAFlow, and *Real*. All noise generation methods are trained on the SIDD training dataset. *Real* represents denoising results from real (not synthetic) noisy-clean paired data in the SIDD training set, serving as an oracle for synthetic noise generation. PNG outperforms other methods

Table 3. Quantitative comparison of DnCNN denoising performance on the PolyU, Nam, SIDD validation, and SIDD+ benchmarks. The percentage (%) denotes the mixing ratio between the two training subsets. The best and second-best results are highlighted in **bold** and underline.

Models	Methods	PolyU		Nam		SIDD Validation		SIDD+		Average	
		PSNR \uparrow	SSIM \uparrow								
DnCNN	<i>Real</i> (100%)	36.34	0.9204	35.35	0.8828	<u>37.72</u>	0.8905	35.68	0.8860	36.27	0.8949
	NeCA-W (100%)	36.96	0.9544	35.61	0.9403	36.26	0.8812	35.42	0.8900	36.06	0.9165
	NAFlow (100%)	36.85	0.9499	37.45	0.9524	37.27	0.8989	36.67	0.9249	37.06	0.9315
	Ours (100%)	<u>37.93</u>	<u>0.9609</u>	<u>38.08</u>	0.9630	37.63	0.8960	36.23	0.9072	<u>37.47</u>	<u>0.9318</u>
	NeCA-W-Mixed (50%)	37.92	0.9601	37.86	0.9580	37.51	0.8952	35.79	0.8961	37.27	0.9274
	NAFlow-Mixed (50%)	37.29	0.9520	37.47	0.9538	37.66	<u>0.9043</u>	36.27	0.9105	37.17	0.9301
	Ours-Mixed (50%)	37.98	0.9610	38.09	<u>0.9617</u>	37.96	0.9047	<u>36.57</u>	<u>0.9137</u>	37.65	0.9353

and surpasses NAFlow by over 0.33 dB in PSNR and 0.002 in SSIM. Notably, the denoising result produced by PNG closely matches that of *Real*, achieving a minimal PSNR gap of only 0.08 dB and surpassing SSIM by 0.001, indicating the high realism of the generated images. The qualitative evaluation is depicted in Fig. 5.

Robustness on Various Real-World Datasets. To further assess denoising performance in real-world scenarios, we train DnCNN with our synthetic dataset and then evaluate them on five additional benchmarks: PolyU, Nam, SIDD validation, and SIDD+. These datasets cover a broad range of noise characteristics. Tab. 3 compares our results with three baselines: NeCA-W and NAFlow, which are trained on synthetic noise, and *Real*, which uses the ground-truth noisy-clean pairs from the SIDD training set. We also report results from mixed training sets that combine equal amounts of real and synthetic data to further enhance performance and improve the practical applicability of synthetic data generation.

Denoising networks trained with our synthetic dataset achieve the best average performance in both the pure synthetic setting (100%) and the mixed setting (50%). In the pure setting, it matches or surpasses *Real* on the smartphone-based SIDD and SIDD+ benchmarks and shows gains on the DSLR-based PolyU, and Nam datasets. These improvements are likely due to the larger scale and diversity of our generated noise, which helps prevent overfitting to a single domain.

In the mixed setting, performance further improves over the pure synthetic setting and exceeds *Real* across all four benchmarks. This demonstrates that our synthesized dataset enables the denoising network to effectively mitigate overfitting issues while also improving in-distribution performance. These results align with findings in other low-level vision dataset generation tasks, where synthesized datasets have been shown to alleviate overfitting problems due to their limited size of training dataset [5, 22, 38, 58, 66]. Our findings suggest that our method is highly effective for real-world denoising tasks and provides a robust training dataset across diverse real-world imaging conditions.

Table 4. Quantitative results of synthetic noise on the PolyU, Nam, and MAI2021. All methods are trained with SIDD training set. The results are computed with KLD \downarrow and AKLD \downarrow . The best results are shown in **bold**.

Methods	PolyU		Nam		MAI2021		Average	
	KLD \downarrow	AKLD \downarrow						
Metadata-Dependent	\times	\times	\times	\times	\times	\times	\times	\times
NAFlow	0.2304	1.7801	0.2055	1.9320	0.7304	2.6465	0.3888	2.1195
Ours	0.0822	0.5814	0.0966	0.4668	0.0747	0.3314	0.0845	0.4599

4.3. Application: Metadata-Free Noise Generation

To demonstrate the effectiveness of our approach, we perform an additional experiment in which metadata are absent or incompatible across datasets. As in the previous section, we compare both noise quality and denoising performance obtained with the synthesized data.

Metadata-Free Noise Quality Assessment. In Tab. 4, we validate the robustness of our method by evaluating the noise quality on external real-world datasets that were not used during the training phase. We compare our PNG with NAFlow trained on SIDD training dataset. We evaluate using three external datasets: PolyU, Nam, MAI2021 [15] (no metadata or inconsistent metadata). These datasets were captured using various device types, camera sensors, and ISPs (*e.g.*, smartphones, and DSLRs). Note that metadata-dependent methods (*e.g.*, NoiseFlow, Flow-sRGB, NeCA-W) are unable to generate noisy images on external datasets where metadata is either unavailable or inconsistent with the metadata used during training. To produce synthetic noisy images, real clean-noisy pairs of each external dataset are passed through PNG. Notably, NAFlow and our method can synthesize noisy images using noisy-clean pairs from the external datasets without metadata. However, unlike our approach, NAFlow still requires metadata for training. The overall results demonstrate that PNG consistently outperforms NAFlow across all datasets, achieving substantial gains in average KLD and AKLD scores. This emphasizes the robustness of PNG on external datasets across various camera settings, demonstrating the potential to expand dataset volume by generating noisy images from limited external datasets.

Table 5. Denoising results on external dataset.

Test Dataset	<i>Real</i> (100%)		NAFlow-Mixed (50%)		Ours-Mixed (50%)	
	PSNR \uparrow	SSIM \uparrow	PSNR \uparrow	SSIM \uparrow	PSNR \uparrow	SSIM \uparrow
Nam	38.87	0.9712	39.69	0.9715	40.40	0.9761

Table 6. Quantitative results of metadata classification on SIDD validation with different combinations of prompts in terms of accuracy \uparrow . We test the validity of the prompts in two aspects: camera sensor type and ISO level. The best and second-best results are highlighted in **bold** and underline.

Classifier	<i>Camera Sensor</i> (%)	<i>Camera Sensor + ISO Level</i>	
		Top-1 (%)	Top-3 (%)
Baseline (No Prompt)	75.80	66.27	93.91
GPB	<u>82.37</u>	<u>68.35</u>	<u>94.71</u>
GPB + LPB	94.47	75.48	98.64

Denoising Results on External Dataset. In Tab. 5, we evaluate the generalization performance of our approach. Specifically, we use PNG trained on SIDD to augment an external dataset (NAM), then train a DnCNN using this augmented data and evaluate the denoising performance. For a fair comparison, we follow the same procedure using NAFlow trained on the same SIDD dataset. The Nam dataset is divided into generation and evaluation subsets at a 4:1 ratio, and the real clean-noisy pairs in the generation subset are passed through PNG, to produce additional synthetic noisy images. When combined with real data, our denoiser trained with 50% real and 50% synthetic data (Ours-Mixed) exceeds the *Real* baseline by 1.53 dB in PSNR and 0.0049 in SSIM, outperforming NAFlow by 0.71 dB and 0.0046 on NAM evaluation subset. *Real* shows denoising results from training DnCNN solely on real datasets. Overall, the results confirm that our unified framework can synthesize realistic noisy data from unseen domains, and incorporating these synthetic samples with real observations boosts denoising accuracy while reducing overfitting.

4.4. Ablation Study

In this section, we provide ablation studies on metadata classification, GPB, and LPB. Due to space limitations, please refer to Sec. S.4 for more comprehensive ablation studies.

Metadata Classification We evaluate the extent to which the prompts extracted from the Prompt Encoder \mathcal{E} capture the characteristics of the input noise.

First, we trained ResNet-based classifiers using either the input noise \mathbf{n}_{Real} or the prompt features as input, measuring their ability to accurately categorize camera sensor types (*i.e.* camera manufacturer). We selected five major camera sensors from the SIDD dataset, resulting in five distinct labels, denoted as *Camera Sensor* in the second column of Tab. 6. The classification results show that using features of GPB as input improves camera sensor prediction accuracy compared to the baseline model, which uses real noise as

Table 7. Effect of GPB and LPB on SIDD validation noise generation. The best results are shown in **bold**.

Combination		Generation	
GPB	LPB	KLD \downarrow	AKLD \downarrow
\times	\times	0.6182	0.4387
\checkmark	\times	0.0287	0.1112
\checkmark	\checkmark	0.0261	0.1108

input (without GPB and LPB). Furthermore, combining GPB with LPB further enhances classification accuracy. These results demonstrate that the prompts contain information about the camera sensor.

Next, we created a total of 16 labels by simultaneously considering these five sensors and additional ISO levels, and conducted classification experiments. We compared their classification performance on the SIDD validation set, measuring Top-1 and Top-3 accuracy (last two columns in Tab. 6). The results show that using both GPB and LPB achieves the best classification performance for identifying the camera sensor and ISO configuration, highlighting the effectiveness of the proposed prompt blocks in capturing input noise-dependent characteristics.

Effect of GPB and LPB on Noise Generation. To evaluate the impact of the prompts extracted by the GPB and LPB, we conducted experiments, as shown in Tab. 7. The P-DiT model is differently trained with various PAE variants to investigate the effect of each prompt. Combining diverse information from the prompt blocks such as ISO settings and noise correlation enhances the quality of synthesized noise by providing vital input-specific distribution details.

5. Conclusion

In this work, we propose a novel PNG framework to remove the reliance on metadata when generating real-world noise. Our PNG comprises two key components: Prompt Autoencoder (PAE) and Prompt DiT (P-DiT). The PAE encodes input noise, generating a compact latent code and extracting meaningful prompt features at various scales to replace input noise-specific metadata. The P-DiT then synthesizes latent codes using prompts and clean images as conditions. Finally, the generated latent codes are fed into the PAE Decoder alongside clean images to produce realistic noisy images. A key advantage of our method is that it does not require explicit metadata during either the training or testing phases, unlike conventional methods, highlighting its strength in real-world applications. Moreover, experimental results on real-world benchmarks demonstrate that our framework excels in both real-world noise generation and downstream denoising tasks.

References

- [1] Abdelrahman Abdelhamed, Stephen Lin, and Michael S Brown. A high-quality denoising dataset for smartphone cameras. In *CVPR*, 2018. 1, 6
- [2] Abdelrahman Abdelhamed, Marcus A Brubaker, and Michael S Brown. Noise flow: Noise modeling with conditional normalizing flows. In *ICCV*, 2019. 1, 2, 5
- [3] Abdelrahman Abdelhamed, Mahmoud Afifi, Radu Timofte, and Michael S Brown. Ntire 2020 challenge on real image denoising: Dataset, methods and results. In *CVPR*, 2020. 1, 6
- [4] Tom Brown, Benjamin Mann, Nick Ryder, Melanie Subbiah, Jared D Kaplan, Prafulla Dhariwal, Arvind Neelakantan, Pranav Shyam, Girish Sastry, Amanda Askell, et al. Language models are few-shot learners. *NeurIPS*, 2020. 2
- [5] Jianrui Cai, Hui Zeng, Hongwei Yong, Zisheng Cao, and Lei Zhang. Toward real-world single image super-resolution: A new benchmark and a new model. In *ICCV*, 2019. 7
- [6] Liangyu Chen, Xin Lu, Jie Zhang, Xiaojie Chu, and Chengpeng Chen. Hinet: Half instance normalization network for image restoration. In *CVPR*, 2021. 1
- [7] Liangyu Chen, Xiaojie Chu, Xiangyu Zhang, and Jian Sun. Simple baselines for image restoration. In *ECCV*, 2022. 1
- [8] Hamadi Chihaoui and Paolo Favaro. Masked and shuffled blind spot denoising for real-world images. In *CVPR*, 2024. 2
- [9] Jia Deng, Wei Dong, Richard Socher, Li-Jia Li, Kai Li, and Li Fei-Fei. Imagenet: A large-scale hierarchical image database. In *CVPR*, 2009. 5, 6
- [10] Patrick Esser, Sumith Kulal, Andreas Blattmann, Rahim Entezari, Jonas Müller, Harry Saini, Yam Levi, Dominik Lorenz, Axel Sauer, Frederic Boesel, et al. Scaling rectified flow transformers for high-resolution image synthesis. In *ICML*, 2024. 2
- [11] Zixuan Fu, Lanqing Guo, and Bihan Wen. srgb real noise synthesizing with neighboring correlation-aware noise model. In *CVPR*, 2023. 1, 2, 5, 6, 3
- [12] Kaiming He, Xiangyu Zhang, Shaoqing Ren, and Jian Sun. Deep residual learning for image recognition. In *CVPR*, 2016. 4
- [13] Jonathan Ho, Ajay Jain, and Pieter Abbeel. Denoising diffusion probabilistic models. *NeurIPS*, 2020. 3
- [14] Aapo Hyvärinen and Peter Dayan. Estimation of non-normalized statistical models by score matching. *JMLR*, 2005. 3
- [15] Andrey Ignatov, Kim Byeoung-su, Radu Timofte, and Angeline Pouget. Fast camera image denoising on mobile gpus with deep learning, mobile ai 2021 challenge: Report. In *CVPRW*, 2021. 7
- [16] Geonwoon Jang, Wooseok Lee, Sanghyun Son, and Kyoung Mu Lee. C2n: Practical generative noise modeling for real-world denoising. In *ICCV*, 2021. 2, 6
- [17] Tero Karras, Timo Aila, Samuli Laine, and Jaakko Lehtinen. Progressive growing of gans for improved quality, stability, and variation. In *ICLR*, 2018. 2
- [18] Tero Karras, Miika Aittala, Timo Aila, and Samuli Laine. Elucidating the design space of diffusion-based generative models. *NeurIPS*, 2022. 3, 2
- [19] Tero Karras, Miika Aittala, Jaakko Lehtinen, Janne Hellsten, Timo Aila, and Samuli Laine. Analyzing and improving the training dynamics of diffusion models. In *CVPR*, 2024. 2, 3
- [20] Dongjin Kim, Donggoo Jung, Sungyong Baik, and Tae Hyun Kim. srgb real noise modeling via noise-aware sampling with normalizing flows. In *ICLR*, 2024. 1, 2, 5, 6, 3
- [21] Dongjin Kim, Jaekyun Ko, Muhammad Kashif Ali, and Tae Hyun Kim. Idf: Iterative dynamic filtering networks for generalizable image denoising. In *ICCV*, 2025. 1
- [22] Hyeonjae Kim, Dongjin Kim, Eugene Jin, and Tae Hyun Kim. Continuous degradation modeling via latent flow matching for real-world super-resolution. In *AAAI*, 2026. 1, 7
- [23] Diederik Kingma, Tim Salimans, Ben Poole, and Jonathan Ho. Variational diffusion models. *NeurIPS*, 2021. 3
- [24] Diederik P Kingma and Jimmy Ba. Adam: A method for stochastic optimization. *arXiv preprint arXiv:1412.6980*, 2014. 5
- [25] Fei Kong, Jinhao Duan, Lichao Sun, Hao Cheng, Renjing Xu, Hengtao Shen, Xiaofeng Zhu, Xiaoshuang Shi, and Kaidi Xu. Act-diffusion: Efficient adversarial consistency training for one-step diffusion models. In *CVPR*, 2024. 3
- [26] Shayan Kousha, Ali Maleky, Michael S Brown, and Marcus A Brubaker. Modeling srgb camera noise with normalizing flows. In *CVPR*, 2022. 1, 2, 6, 5
- [27] Wooseok Lee, Sanghyun Son, and Kyoung Mu Lee. Apbsn: Self-supervised denoising for real-world images via asymmetric pd and blind-spot network. In *CVPR*, 2022. 2
- [28] Bingchen Li, Xin Li, Yiting Lu, Ruoyu Feng, Mengxi Guo, Shijie Zhao, Li Zhang, and Zhibo Chen. Promptcir: blind compressed image restoration with prompt learning. In *CVPRW*, 2024. 2
- [29] Xin Li, Bingchen Li, Yeying Jin, Cuiling Lan, Hanxin Zhu, Yulin Ren, and Zhibo Chen. Ucip: A universal framework for compressed image super-resolution using dynamic prompt. In *ECCV*, 2024.
- [30] Zilong Li, Yiming Lei, Chenglong Ma, Junping Zhang, and Hongming Shan. Prompt-in-prompt learning for universal image restoration. *arXiv preprint arXiv:2312.05038*, 2023. 2
- [31] Xinqi Lin, Jingwen He, Ziyang Chen, Zhaoyang Lyu, Bo Dai, Fanghua Yu, Yu Qiao, Wanli Ouyang, and Chao Dong. Diffbir: Toward blind image restoration with generative diffusion prior. In *ECCV*, 2024. 3
- [32] Liyuan Liu, Haoming Jiang, Pengcheng He, Weizhu Chen, Xiaodong Liu, Jianfeng Gao, and Jiawei Han. On the variance of the adaptive learning rate and beyond. In *ICLR*, 2020. 5
- [33] Ilya Loshchilov and Frank Hutter. Sgdr: Stochastic gradient descent with warm restarts. *arXiv preprint arXiv:1608.03983*, 2017. 5
- [34] Chunjie Luo, Jianfeng Zhan, Xiaohe Xue, Lei Wang, Rui Ren, and Qiang Yang. Cosine normalization: Using cosine similarity instead of dot product in neural networks. In *ICANN*, 2018. 2
- [35] Simian Luo, Yiqin Tan, Longbo Huang, Jian Li, and Hang Zhao. Latent consistency models: Synthesizing high-resolution images with few-step inference. *arXiv preprint arXiv:2310.04378*, 2023. 2, 3

- [36] Seonghyeon Nam, Youngbae Hwang, Yasuyuki Matsushita, and Seon Joo Kim. A holistic approach to cross-channel image noise modeling and its application to image denoising. In *CVPR*, 2016. 1, 6
- [37] Yizhong Pan, Xiao Liu, Xiangyu Liao, Yuanzhouhan Cao, and Chao Ren. Random sub-samples generation for self-supervised real image denoising. In *ICCV*, 2023. 2
- [38] Seobin Park, Dongjin Kim, Sungyong Baik, and Tae Hyun Kim. Learning controllable degradation for real-world super-resolution via constrained flows. In *ICML*, 2023. 1, 7
- [39] William Peebles and Saining Xie. Scalable diffusion models with transformers. In *ICCV*, 2023. 2, 5, 1, 3
- [40] Ethan Perez, Florian Strub, Harm De Vries, Vincent Dumoulin, and Aaron Courville. Film: Visual reasoning with a general conditioning layer. In *AAAI*, 2018. 1
- [41] Tobias Plotz and Stefan Roth. Benchmarking denoising algorithms with real photographs. In *CVPR*, 2017. 1
- [42] Vaishnav Potlapalli, Syed Waqas Zamir, Salman Khan, and Fahad Khan. PromptIR: Prompting for all-in-one image restoration. In *NeurIPS*, 2023. 2
- [43] Robin Rombach, Andreas Blattmann, Dominik Lorenz, Patrick Esser, and Björn Ommer. High-resolution image synthesis with latent diffusion models. In *CVPR*, 2022. 3
- [44] Robin Rombach, Andreas Blattmann, Dominik Lorenz, Patrick Esser, and Björn Ommer. High-resolution image synthesis with latent diffusion models. In *CVPR*, 2022. 5
- [45] Olaf Ronneberger, Philipp Fischer, and Thomas Brox. U-net: Convolutional networks for biomedical image segmentation. In *MICCAI*, 2015. 3
- [46] Timo Schick and Hinrich Schütze. Exploiting cloze-questions for few-shot text classification and natural language inference. In *EACL*, 2021. 2
- [47] Wenzhe Shi, Jose Caballero, Ferenc Huszár, Johannes Totz, Andrew P Aitken, Rob Bishop, Daniel Rueckert, and Zehan Wang. Real-time single image and video super-resolution using an efficient sub-pixel convolutional neural network. In *CVPR*, 2016. 5
- [48] Taylor Shin, Yasaman Razeghi, Robert L. Logan IV, Eric Wallace, and Sameer Singh. AutoPrompt: Eliciting knowledge from language models with automatically generated prompts. In *EMNLP*, 2020. 2
- [49] Jascha Sohl-Dickstein, Eric Weiss, Niru Maheswaranathan, and Surya Ganguli. Deep unsupervised learning using nonequilibrium thermodynamics. In *ICML*, 2015. 3
- [50] Yang Song and Prafulla Dhariwal. Improved techniques for training consistency models. In *ICLR*, 2024. 3, 5, 2
- [51] Yang Song and Stefano Ermon. Generative modeling by estimating gradients of the data distribution. *NeurIPS*, 2019. 3
- [52] Yang Song and Stefano Ermon. Improved techniques for training score-based generative models. *NeurIPS*, 2020.
- [53] Yang Song, Jascha Sohl-Dickstein, Diederik P Kingma, Abhishek Kumar, Stefano Ermon, and Ben Poole. Score-based generative modeling through stochastic differential equations. In *ICLR*, 2021. 3
- [54] Yang Song, Prafulla Dhariwal, Mark Chen, and Ilya Sutskever. Consistency models. In *ICML*, 2023. 2, 3
- [55] A Vaswani. Attention is all you need. *NeurIPS*, 2017. 1
- [56] Cong Wang, Jinshan Pan, Wei Wang, Jiangxin Dong, Mengzhu Wang, Yakun Ju, and Junyang Chen. Promptrestorer: A prompting image restoration method with degradation perception. *NeurIPS*, 2024. 2
- [57] Tao Wang, Wanglong Lu, Kaihao Zhang, Wenhan Luo, Taekyun Kim, Tong Lu, Hongdong Li, and Ming-Hsuan Yang. Promptrr: Diffusion models as prompt generators for single image reflection removal. *arXiv preprint arXiv:2402.02374*, 2024. 2
- [58] Xintao Wang, Liangbin Xie, Chao Dong, and Ying Shan. Real-esrgan: Training real-world blind super-resolution with pure synthetic data. In *ICCV*, 2021. 7
- [59] Zichun Wang, Ying Fu, Ji Liu, and Yulun Zhang. Lg-bpn: Local and global blind-patch network for self-supervised real-world denoising. In *CVPR*, 2023. 2, 4
- [60] Qi Wu, Mingyan Han, Ting Jiang, Haoqiang Fan, Bing Zeng, and Shuaicheng Liu. Realistic noise synthesis with diffusion models. *arXiv preprint arXiv:2305.14022*, 2023. 2
- [61] Rongyuan Wu, Lingchen Sun, Zhiyuan Ma, and Lei Zhang. One-step effective diffusion network for real-world image super-resolution. *NeurIPS*, 2024. 3
- [62] Rongyuan Wu, Tao Yang, Lingchen Sun, Zhengqiang Zhang, Shuai Li, and Lei Zhang. Seesr: Towards semantics-aware real-world image super-resolution. In *CVPR*, 2024. 3
- [63] Zhijian Wu, Wenhui Liu, Jingchao Wang, Jun Li, and Dingjiang Huang. Freprompter: Frequency self-prompt for all-in-one image restoration. *Pattern Recognition*, 2025. 2
- [64] Bin Xia, Yulun Zhang, Shiyin Wang, Yitong Wang, Xinglong Wu, Yapeng Tian, Wenming Yang, and Luc Van Gool. Diffir: Efficient diffusion model for image restoration. In *ICCV*, pages 13095–13105, 2023. 3
- [65] Jun Xu, Hui Li, Zhetong Liang, David Zhang, and Lei Zhang. Real-world noisy image denoising: A new benchmark. *arXiv preprint arXiv:1804.02603*, 2018. 1, 6
- [66] Tao Yang, Peiran Ren, Lei Zhang, et al. Synthesizing realistic image restoration training pairs: A diffusion approach. *arXiv preprint arXiv:2303.06994*, 2023. 7
- [67] Zongsheng Yue, Qian Zhao, Lei Zhang, and Deyu Meng. Dual adversarial network: Toward real-world noise removal and noise generation. In *ECCV*, 2020. 6
- [68] Syed Waqas Zamir, Aditya Arora, Salman Khan, Munawar Hayat, Fahad Shahbaz Khan, Ming-Hsuan Yang, and Ling Shao. Cycleisp: Real image restoration via improved data synthesis. In *CVPR*, 2020. 1, 2
- [69] Syed Waqas Zamir, Aditya Arora, Salman Khan, Munawar Hayat, Fahad Shahbaz Khan, Ming-Hsuan Yang, and Ling Shao. Learning enriched features for real image restoration and enhancement. In *ECCV*, 2020. 1
- [70] Syed Waqas Zamir, Aditya Arora, Salman Khan, Munawar Hayat, Fahad Shahbaz Khan, and Ming-Hsuan Yang. Restormer: Efficient transformer for high-resolution image restoration. In *CVPR*, 2022. 1
- [71] Dan Zhang, Fangfang Zhou, Yuwen Jiang, and Zhengming Fu. Mm-bsn: Self-supervised image denoising for real-world with multi-mask based on blind-spot network. In *CVPRW*, 2023. 2

- [72] Kai Zhang, Wangmeng Zuo, Yunjin Chen, Deyu Meng, and Lei Zhang. Beyond a gaussian denoiser: Residual learning of deep cnn for image denoising. *IEEE TIP*, 2017. [5](#)
- [73] Kaiyang Zhou, Jingkang Yang, Chen Change Loy, and Ziwei Liu. Learning to prompt for vision-language models. *IJCV*, 2022. [2](#)
- [74] Muzhi Zhu, Hengtao Li, Hao Chen, Chengxiang Fan, Weian Mao, Chenchen Jing, Yifan Liu, and Chunhua Shen. Seg-prompt: Boosting open-world segmentation via category-level prompt learning. In *ICCV*, 2023. [2](#)
- [75] Yunhao Zou, Chenggang Yan, and Ying Fu. Iterative denoiser and noise estimator for self-supervised image denoising. In *ICCV*, 2023. [2](#)

Diffusion-Based sRGB Real Noise Generation via Prompt-Driven Noise Representation Learning

Supplementary Material

Contents

1. Introduction	1
2. Related Works	2
3. Proposed Method	3
3.1. Preliminaries	3
3.2. Overall Flow: PNG	3
3.3. Prompt Autoencoder	4
3.3.1 . Prompt Encoder	4
3.3.2 . Decoder	5
3.4. Prompt DiT (P-DiT)	5
4. Experiments	5
4.1. Experimental Setup	5
4.2. Real-World sRGB Noise Generation and Re- removal	6
4.3. Application: Metadata-Free Noise Generation	7
4.4. Ablation Study	8
5. Conclusion	8
S. Supplementary Material	1
S.1. Prompt DiT	1
S.2. Training details of P-DiT	2
S.2.1 . CM Parameterization	2
S.2.2 . CM Hyperparamters	2
S.2.3 . Latent Code Normalization	3
S.2.4 . P-DiT Hyperparamters	3
S.3. Model Size and Inference Speed of PNG	3
S.4. Additional Ablation Studies	4
S.4.1 . Effect of Conditioning Features in P- DiT	4
S.4.2 . Effect of GPB and LPB on Noisy Im- age Reconstruction	4
S.4.3 . Effect of Number of P-DiT Blocks	4
S.5. Further Analysis of the Generalization Perfor- mance	4
S.6. Unpaired Noise Generation	5
S.6.1 . Generated Noise Quality Assessment.	5
S.6.2 . Denoising Quality Assessment.	5
S.7. Qualitative Results of Noise Generation	6
S.8. Qualitative Results of Denoising Performance	6

S. Supplementary Material

S.1. Prompt DiT

In Fig. 2 and Fig. S1, we introduce P-DiT, which fully leverages the prompt features extracted from the Prompt Encoder \mathcal{E} to synthesize latent codes that align with the embedded information of the input noise characteristics. Our P-DiT is based on DiT [39], a transformer-based CM architecture specifically designed for training diffusion models.

In Fig. S1 (a), the P-DiT consists of a series of B P-DiT blocks through which the noise-added input latent \mathbf{z}_{t+1} is processed. Moreover, for conditioning features, we use the timestep $t + 1$, clean images $\mathcal{I}_{\text{Clean}}$, and prompt features $\mathbf{F}_{\text{Local}}$ and $\mathbf{F}_{\text{Global}}$. The timestep enables the model to adjust its denoising predictions based on the noise levels of the diffusion process at each timestep. Precisely, the timestep is embedded by a timestep embedder, composed of sinusoidal embeddings and an MLP block [55]. We also use the clean image to help the model learn the signal-dependent properties of real-world noise and prompt features to learn the camera-dependent properties. This enables the generation of latent codes that capture input noise characteristics without relying on metadata, with these features embedded by a conditional embedder. Specifically, we first downsample these inputs to match the spatial size of the latent codes and then extract shallow features separately using 3×3 convolutional layers, which are concatenated along the channel axis as follows:

$$\mathbf{F}_{\text{Cond}} = \left[\left[\text{Conv}_{3 \times 3}(\text{PD}(\mathcal{I}_{\text{Clean}})), \text{Conv}_{3 \times 3}(\text{PD}(\mathbf{F}_{\text{Local}})), \right. \right. \\ \left. \left. \text{Conv}_{3 \times 3}(\text{PD}(\mathbf{F}_{\text{Global}})) \right] \right], \quad (\text{S1})$$

where $\text{PD}(\cdot)$ indicates a pixel downsampling operator. Note that we use $\mathbf{F}_{\text{Global}}$ for all scale levels, and each feature is processed separately. The concatenated feature \mathbf{F}_{Cond} is then processed with global average pooling and added to the time embeddings.

In Fig. S1 (b), we present the P-DiT block. We employ adaptive layer normalization (AdaLN) as the conditioning mechanism to modulate the statistics of input features. AdaLN consists of two components: layer normalization [40] and adaptive modulation. AdaLN first normalizes the input features to have a mean of zero and a standard deviation of one. Then, the normalized features are modulated using scale and shift parameters derived from the conditioning input.

Moreover, to fully leverage the available information from

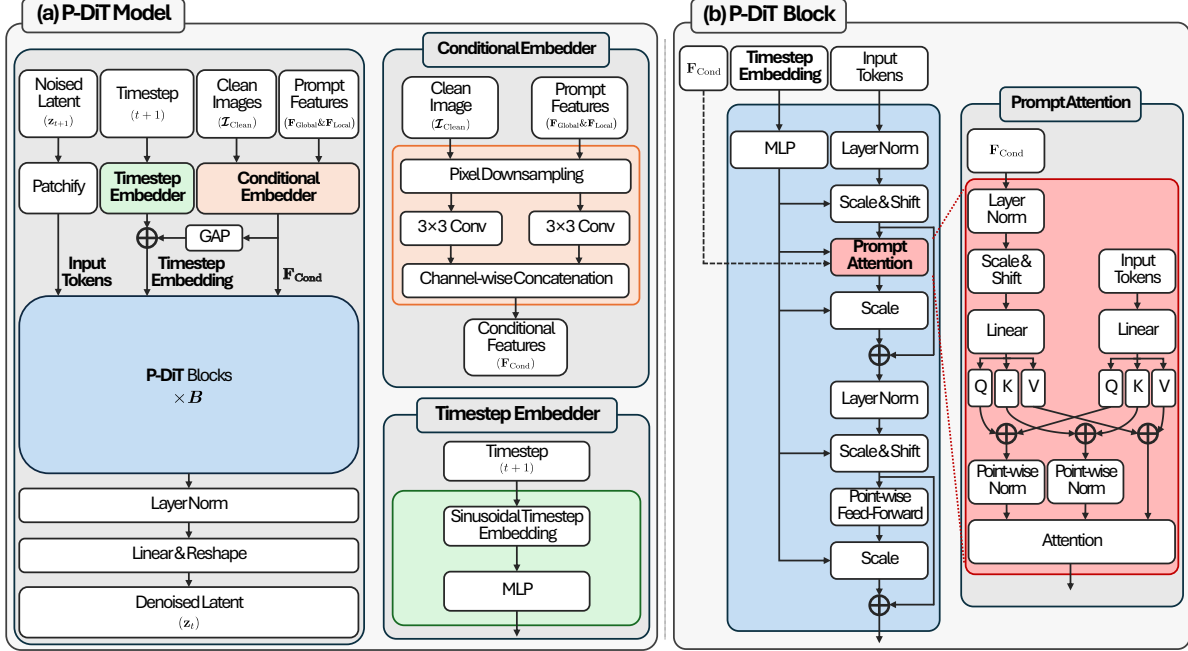


Figure S1. Overview of Prompt DiT (P-DiT). (a) Overall P-DiT structure. (b) P-DiT block.

the conditions and capture locally varying spatial correlations characteristics in prompt features, we further enhance these features through a prompt attention mechanism, referred to as **Prompt Attention**.

Prompt Attention. As illustrated in Fig. S1 (b), we use the conditions to generate the key (K), query (Q), and value (V) within the attention layer by projections, similar to MMDiT [10], enabling the model to effectively capture the spatial information of the prompt features. Specifically, we first modulate the combined conditional features F_{Cond} through AdaLN to extract time-dependent information. Then, we generate the key, query, and value features using a single linear layer and combine them with the corresponding features from the input tokens through element-wise addition. Using these conditioned features, we apply cosine attention [19, 34] with point-wise normalization [17] to stabilize the training process [19].

S.2. Training details of P-DiT

S.2.1. CM Parameterization

The CM-based model f_θ aims to approximate the consistency function $f(\cdot, \cdot)$, which satisfies $f(\mathbf{x}_t, \sigma_t) = \mathbf{x}_0$. Therefore, it must adhere to the boundary condition $f(\mathbf{x}_0, \sigma_0) = \mathbf{x}_0$. To ensure this, we follow the parameterization used in EDM [18] and CM [54], defining the model as follows:

$$f_\theta(\mathbf{x}_t, \sigma_t) = c_{\text{skip}}(\sigma_t)\mathbf{x}_t + c_{\text{out}}(\sigma_t)F_\theta(c_{\text{in}}(\sigma_t)\mathbf{x}_t, \sigma_t), \quad (\text{S2})$$

where F_θ is a free-form neural network, such as P-DiT, and c_{in} , c_{out} , and c_{skip} control the scaling of input, output magnitudes, and the skip connection, respectively. These can be

expressed as:

$$c_{\text{in}}(\sigma_t) = \frac{1}{\sqrt{\sigma_{\text{data}}^2 + \sigma_t^2}}, \quad c_{\text{skip}}(\sigma_t) = \frac{\sigma_{\text{data}}^2}{(\sigma_t - \sigma_0)^2 + \sigma_{\text{data}}^2},$$

$$c_{\text{out}}(\sigma_t) = \frac{\sigma_{\text{data}}(\sigma_t - \sigma_0)}{\sqrt{\sigma_{\text{data}}^2 + \sigma_t^2}}. \quad (\text{S3})$$

These formulations meet the boundary conditions where $c_{\text{skip}}(\sigma_0) = 1$ and $c_{\text{out}}(\sigma_0) = 0$.

S.2.2. CM Hyperparameters

We detail the hyperparameters for training P-DiT, adopting most from iCT [50] for CM.

Discretization Curriculum. The discretization curriculum is designed to enhance CM training by systematically increasing the number of discretization timesteps T in Eq. (1), improving the quality of generated samples. The discretization curriculum $\mathcal{C}(k)$ is defined as follows:

$$\mathcal{C}(k) = \min(s_0 2^{\frac{k}{K'}}, s_1) + 1, \quad \text{where } K' = \left\lceil \frac{K}{\log_2 \frac{s_1}{s_0} + 1} \right\rceil. \quad (\text{S4})$$

In this context, k ranges over $\{0, 1, \dots, K\}$, where K denotes the total number of training iterations. The parameters s_0 and s_1 refer to the minimum and maximum discretization steps, respectively. While iCT [50] uses $s_0 = 10$ and $s_1 = 1280$, we empirically found that setting maximum number of discretization steps s_1 to 160 is sufficient to produce competitive performance.

Noise Schedule. The noise schedule plays a crucial role in determining the sampling of noise levels during the CM

training, significantly influencing the quality of the generated samples. To define the noise schedule, we first discretize the noise level as follows: $\sigma_{\min} = \sigma_0 < \sigma_1 < \dots < \sigma_T = \sigma_{\max}$ where $\sigma_{\min} = 0.002$, $\sigma_{\max} = 80$. As in [18, 50, 54], we set σ_t as:

$$\sigma_t = \left(\sigma_{\min}^{1/\tau} + \frac{t-1}{\mathcal{C}(k)-1} \left(\sigma_{\max}^{1/\tau} - \sigma_{\min}^{1/\tau} \right) \right)^\tau, \quad (\text{S5})$$

where $t \in \{1, 2, \dots, \mathcal{C}(k)\}$. We use $\tau = 7$ and τ controls for the step length between noise levels σ_t and σ_{t+1} . As τ increases, the step length at lower noise levels decreases, allowing the model to better capture high-frequency details.

Additionally, we utilize a lognormal distribution for noise level sampling, which reduces the emphasis on higher noise levels and mitigates the accumulation of errors in CT loss at lower noise levels. The noise sampling schedule is defined as:

$$\sigma_t, \text{ where } t \sim p(t), \text{ and} \\ p(t) \propto \text{erf} \left(\frac{\log(\sigma_{t+1}) - P_{\text{mean}}}{\sqrt{2}P_{\text{std}}} \right) - \text{erf} \left(\frac{\log(\sigma_t) - P_{\text{mean}}}{\sqrt{2}P_{\text{std}}} \right), \quad (\text{S6})$$

where erf indicates error function, and $P_{\text{mean}}, P_{\text{std}}$ determine the shape of log distribution. We choose $P_{\text{mean}} = -1.1$, $P_{\text{std}} = 2.0$, following iCT [50].

Loss Function. In Eq. (1), we use the pseudo-Huber loss [50] as the distance function $d(\cdot)$. The pseudo-Huber loss transitions between \mathcal{L}_1 and \mathcal{L}_2 metrics and is more robust to outliers than the \mathcal{L}_2 metric. The pseudo-Huber loss is defined as:

$$d(\mathbf{x}, \mathbf{y}) = \sqrt{\|\mathbf{x} - \mathbf{y}\|_2^2 + c^2} - c, \quad (\text{S7})$$

where $c = 0.00054\sqrt{m}$, and m indicates data dimensionality.

Loss Weighting. The weighting function $\lambda(\cdot)$ in Eq. (1) modulates the significance of CT losses across varying noise levels during training. As followed by [50], we set the weighting function $\lambda(\cdot)$ as follows:

$$\lambda(\sigma_t) = \frac{1}{\sigma_{t+1} - \sigma_t}. \quad (\text{S8})$$

By assigning lower weights to higher noise levels, the weighting function ensures that the model focuses on learning from lower noise levels, where the data is more distinct and informative. This strategy improves sample quality by reducing the influence of errors associated with higher noise levels, thereby enhancing the overall performance of consistency models.

S.2.3. Latent Code Normalization

The formulation of EDM [18] assumes that the mean and standard deviation of the training data are zero and σ_{data} ,

Table S1. Inference time comparison between NeCA-W, NAFlow, and PNG.

Resolution	Inference Time (image / second)		
	NeCA-W	NAFlow	Ours
256×256	150	13	57
512×512	38	8	21
1024×1024	9	4	5

respectively, as stated in Eq. (S2). Following the approach in [19], we also normalize the encoded latent codes using precomputed statistics from the training data. Specifically, we first calculate the channel-wise mean and standard deviation of the latent codes from the training dataset. Then, we subtract the input latent code by the precomputed mean to achieve a mean of zero, and divide it by the precomputed standard deviation, followed by multiplying by σ_{data} to set the standard deviation to σ_{data} . When the latent codes are generated, we reverse this procedure before transforming them back to the image space via the Decoder \mathcal{D} .

S.2.4. P-DiT Hyperparameters

Following the approach in [50, 54], we update P-DiT parameters using an exponential moving average with a decay rate of 0.9999 to stabilize the training process. P-DiT’s model hyperparameters are based on DiT-S [39], except for the number of blocks ($B = 8$), to improve efficiency. The input noised latent is tokenized with a patch size of 1, allowing for finer noise information to be embedded in the latent code. To mitigate overfitting, we apply a dropout rate of 0.1 to the pointwise feed-forward layer and add minor noise and apply downsampling operation with a factor of 2 to the conditional clean images [54].

S.3. Model Size and Inference Speed of PNG

Our PNG consists of two sub-models, PAE with 14.9M parameters and P-DiT with 29.1M, yielding roughly 44M parameters in total. This total is comparable to NeCA-W [11], whose camera-specific model for each of the five manufacturers in the SIDD dataset contains 40.5M parameters. To train both PAE and P-DiT, we utilize four NVIDIA A6000 GPUs. Following the approach in [18, 19, 50, 54], we train P-DiT using mixed-precision, which reduces both training time and memory consumption.

To evaluate the computational complexity of our two-stage framework, we compare the inference time at different image resolutions with two other SOTA models, NeCA-W [11] and NAFlow [20]. Specifically, we measure the number of images that each model can process per second on a single A6000 GPU. As shown in Tab. S1, with a resolution of 256×256, PNG can generate 57 images per second, which is about 4.38 times faster than NAFlow. At a 512×512 resolution, PNG generates 21 images per second,

Table S2. Effect of conditioning features on different components in P-DiT. The best results are shown in **bold**.

Conditioning		Generation	
Timestep	Attention	KLD↓	AKLD↓
✗	✗	0.5661	0.4132
✓	✗	0.0287	0.1291
✓	✓	0.0261	0.1108

Table S3. Effect of GPB and LPB on SIDD validation noisy image reconstruction. The best results are shown in **bold**.

Combination		Reconstruction	
GPB	LPB	PSNR↑	SSIM↑
✗	✗	37.58	0.9800
✓	✗	46.30	0.9982
✓	✓	46.54	0.9983

2.625 times faster than NAFlow. At the highest resolution of 1024×1024 , PNG still performs 1.25 times faster than NAFlow, producing 5 images per second, demonstrating its practicality at high image resolutions. Even though NeCA-W shows the highest speed at all resolutions, the inference time difference ratio between NeCA-W and PNG decreases as the resolution increases, from 2.63 to 1.8. Hence, our method demonstrates strong performance while maintaining reasonable computational complexity at high resolutions compared to recent SOTA models.

S.4. Additional Ablation Studies

S.4.1. Effect of Conditioning Features in P-DiT

P-DiT generates latent codes that embed noise information through conditional features. Specifically, in Fig. S1 (a), we first add the conditional feature \mathbf{F}_{Cond} to the timestep embedding, and in Fig. S1 (b), we condition the conditional feature through prompt attention.

In Tab. S2, we investigate the effect of conditional features on two different components: the timestep embedding and attention. P-DiT without any conditional features fails to capture the target noise information, resulting in inferior performance in terms of KLD and AKLD. The model that conditions the conditional features on both components demonstrates superior performance compared to the model that only conditions them on the timestep embedding. This highlights that utilizing spatial information through the proposed prompt attention allows the model to fully exploit the conditional features.

Table S4. KLD score depending on different number of blocks B .

# Blocks	KLD↓
$B = 4$	0.0350
$B = 6$	0.0345
$B = 8$	0.0261

S.4.2. Effect of GPB and LPB on Noisy Image Reconstruction

In Tab. S3, we also assess the influence of both prompt blocks on noisy image reconstruction. Incorporating GPB and LPB enhances the fidelity of the reconstructed images, as the prompt features encompass meaningful information about noise characteristics at different scales (see Fig. 3). Therefore, it is essential to utilize both prompt features to enhance the quality of the reconstructed images. In particular, we pass the latent directly from the Prompt Encoder \mathcal{E} to the Decoder \mathcal{D} , without using P-DiT for this experiment.

S.4.3. Effect of Number of P-DiT Blocks

As shown in Tab. S4, we measure the KLD scores across different numbers of blocks B in the P-DiT to evaluate their impact on noise generation, with B representing the hierarchical levels used in our P-DiT. The results indicate that increasing the number of blocks improves the quality of noise generation. Even with half the number of blocks, P-DiT yet achieves a moderate KLD score, with only a slight difference from the final version ($B=8$), suggesting an opportunity to optimize the trade-off between model complexity and performance.

S.5. Further Analysis of the Generalization Performance

As shown in Tab. 3, denoising networks trained with our synthesized dataset exhibit strong robustness to unseen noise. We further conduct experiments to assess the generalization capability of our approach on external datasets. The results demonstrate that expanding the training dataset through synthetic image generation helps mitigate overfitting to the training distribution and leads to improved performance on external dataset.

For the experiments, we select 15,000 non-overlapping patches from the SIDD training set to generate synthetic noisy images to train the DnCNN network. This setup ensures that each noisy sample is unique, providing a controlled environment to systematically analyze the impact of the size of the dataset on generalization.

In Tab. S5, we organize the training data into three distinct groups: $\times 1$, $\times 2$, and $\times 4$, where each factor indicates the number of synthetic noisy samples generated per clean image using PNG. Importantly, performance on the in-distribution dataset (SIDD+) remains consistent across

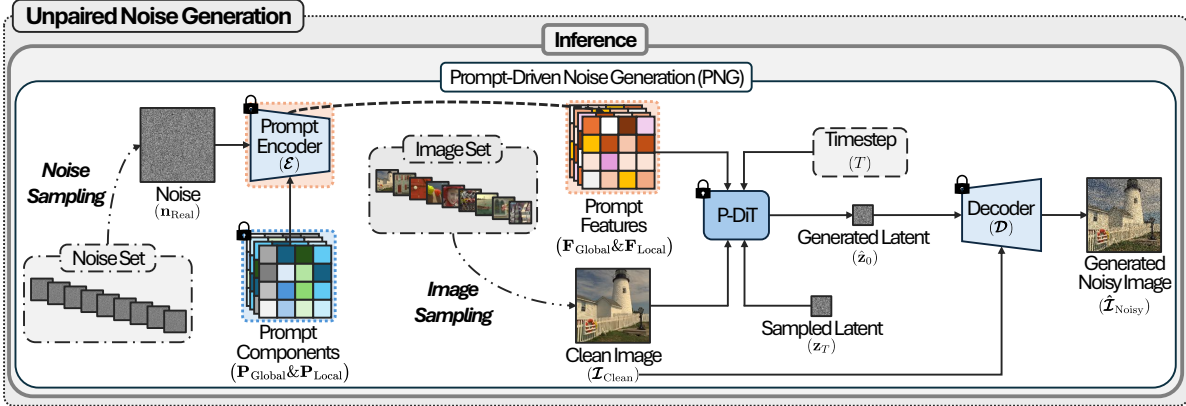


Figure S2. Overview of unpaired noise generation process.

Table S5. Quantitative results on denoising generalization performance depending on the size of the synthesized dataset using PNG. The multiplication sign (\times) indicates the scaling applied to the original number of patches. The best and second-best results are denoted as **bold** and underline, respectively.

# Samples	PolyU		Nam		SIDD Validation		SIDD+		Average	
	PSNR \uparrow	SSIM \uparrow								
$\times 1$	37.40	0.9569	37.29	0.9578	36.55	<u>0.8887</u>	35.72	0.8997	36.74	0.9258
$\times 2$	<u>37.61</u>	<u>0.9546</u>	<u>37.92</u>	0.9580	<u>36.95</u>	0.8838	<u>35.87</u>	0.9078	<u>37.09</u>	<u>0.9260</u>
$\times 4$	37.72	0.9542	37.94	<u>0.9578</u>	37.27	0.8955	36.00	<u>0.9022</u>	37.23	0.9274

all groups. However, the denoising network’s robustness on external datasets improves as the number of training samples increases, with the $\times 4$ group achieving the highest average performance. These findings suggest that increasing noise diversity through synthetic data generation effectively reduces overfitting and highlights the efficacy of the PNG approach.

S.6. Unpaired Noise Generation

In Tab. 1, we use paired noisy image $\mathcal{I}_{\text{Noisy}}$ and clean image $\mathcal{I}_{\text{Clean}}$ from test datasets during inference to compute $\mathbf{n}_{\text{Real}} = \mathcal{I}_{\text{Clean}} - \mathcal{I}_{\text{Noisy}}$, following the experimental setup used in previous works [2, 11, 20, 26]. To broaden PNG’s applicability to cases where only some noisy-clean pairs are available for training alongside extra clean-only images, we also evaluate it in an unpaired setting. In this scenario, as illustrated in Fig. S2, noise images \mathbf{n}_{Real} are randomly sampled from the training dataset (e.g. SIDD) and used to synthesize noisy images $\hat{\mathcal{I}}_{\text{Noisy}}$ conditioned on new, unpaired clean images $\mathcal{I}_{\text{Clean}}$ that are randomly sampled from the external dataset (e.g. ImageNet [9]), during the inference.

S.6.1. Generated Noise Quality Assessment.

Experiment Settings. In Tab. S6, we evaluate noise quality under the same unpaired setting as described above, using NAFlow, NeCA-W, and PNG. All models are trained on the paired SIDD training dataset, and NeCA-W and NAFlow are evaluated using their official weights as described in Sec. 4.2 of the main manuscript. To evaluate how well noise genera-

tion networks model each specific noise domains with SIDD validation, we categorize results by different five smartphone types. Notably, in this table, we use metadata only for categorization; however, in real-world applications, our method can synthesize a dataset following the trained noise distribution without relying on any metadata.

Noise Quality Results. Tab. S6 shows that, while the unpaired setting introduces a slight performance drop compared to the paired setting, PNG still achieves comparable or superior noise quality metrics (KLD and AKLD) compared to other baseline methods such as NeCA-W and NAFlow. Furthermore, PNG achieves even superior performance compared to NeCA-W in the paired setting (KLD: 0.0342, AKLD: 0.1436), despite utilizing limited noise information. This flexibility underscores the adaptability of PNG, which synthesizes realistic noisy images without requiring paired clean-noisy images.

This makes PNG also suitable for scenarios where paired datasets are unavailable. Additionally, in the paired setting, PNG demonstrates strong performance without the need for explicitly defined metadata such as ISO or camera type. These results further support the practicality of PNG across a wide range of use cases, regardless of whether paired or unpaired data are available.

S.6.2. Denoising Quality Assessment.

Experiment Settings. To further assess the quality of generated noise, we train the DnCNN model only using noisy

Table S6. Quantitative results for the noise generation performance on SIDD validation set under unpaired settings. The results are reported using KLD↓ and AKLD↓, with the best and second-best results highlighted in **bold** and underline, respectively. † indicates that the model is evaluated under an unpaired setting.

Methods	G4		GP		IP		N6		S6		Average	
	KLD↓	AKLD↓										
NeCA-W†	<u>0.0513</u>	<u>0.1765</u>	<u>0.0487</u>	<u>0.1819</u>	<u>0.0258</u>	<u>0.1609</u>	<u>0.0603</u>	<u>0.1496</u>	<u>0.0581</u>	<u>0.2205</u>	<u>0.0489</u>	<u>0.1779</u>
NAFlow†	0.4482	1.6918	0.2260	1.0135	0.3267	1.1612	0.2200	0.8725	0.1462	0.5456	0.2734	1.0569
Ours†	0.0350	0.1567	0.0312	0.1553	0.0222	0.1392	0.0291	0.1229	0.0204	0.1326	0.0276	0.1413

Table S7. Quantitative results on denoising generalization performance trained with synthetic noisy-clean pairs generated in an unpaired manner. The best and second-best results are denoted as **bold** and underline, respectively. † indicates that noise is generated under an unpaired setting.

Methods	PolyU		Nam		SIDD Validation		SIDD+		Average	
	PSNR↑	SSIM↑	PSNR↑	SSIM↑	PSNR↑	SSIM↑	PSNR↑	SSIM↑	PSNR↑	SSIM↑
NeCA-W†	<u>37.39</u>	<u>0.9555</u>	<u>37.13</u>	<u>0.9495</u>	<u>32.86</u>	<u>0.7490</u>	<u>33.92</u>	<u>0.8342</u>	<u>35.33</u>	<u>0.8720</u>
NAFlow†	32.40	0.9157	31.73	0.9381	30.89	0.7776	31.60	0.7953	31.66	0.8567
Ours†	38.00	0.9618	38.37	0.9633	32.93	0.7803	34.25	0.8557	35.89	0.8903

images generated via an unpaired approach. To ensure a rigorous assessment, we randomly select noise from 15,000 non-overlapping patches from the SIDD training set and randomly paired these with clean images from the ImageNet [9] validation set, which contains 50,000 images from various scenes. Subsequently, 50,000 synthetic noisy-clean image pairs are generated from the ImageNet dataset.

Denoising Results. As shown in Tab. S7, the DnCNN model trained on our method outperforms SOTA methods, including NeCA-W and NAFlow, across all real-world datasets. These results confirm the superior performance of unpaired noise generation with PNG. Specifically, these denoising results are consistent with the unpaired noise generation results in Table S6, where NAFlow produces the lowest denoising performance, which can be attributed to its lower-quality unpaired noise generation. NeCA-W achieves the second-best denoising results, but our method surpasses NeCA-W, with average improvements of 0.56 in PSNR and 0.0183 in SSIM. In summary, compared to recent SOTA methods such as NeCA-W and NAFlow, our approach is capable of generating high-quality noise in both paired and unpaired scenarios, demonstrating its practicality for real-world applications.

S.7. Qualitative Results of Noise Generation

In Fig. S3, we provide additional visualizations of generated noise, comparing our method (PNG) with other approaches: C2N [16], NeCA-W [11], and NAFlow [20].

S.8. Qualitative Results of Denoising Performance

In Fig. S4, we provide additional visualizations of denoising results, where the denoising network is trained on synthetic datasets. We compare our method (PNG) with other ap-

proaches, including C2N, NeCA-W, and NAFlow.

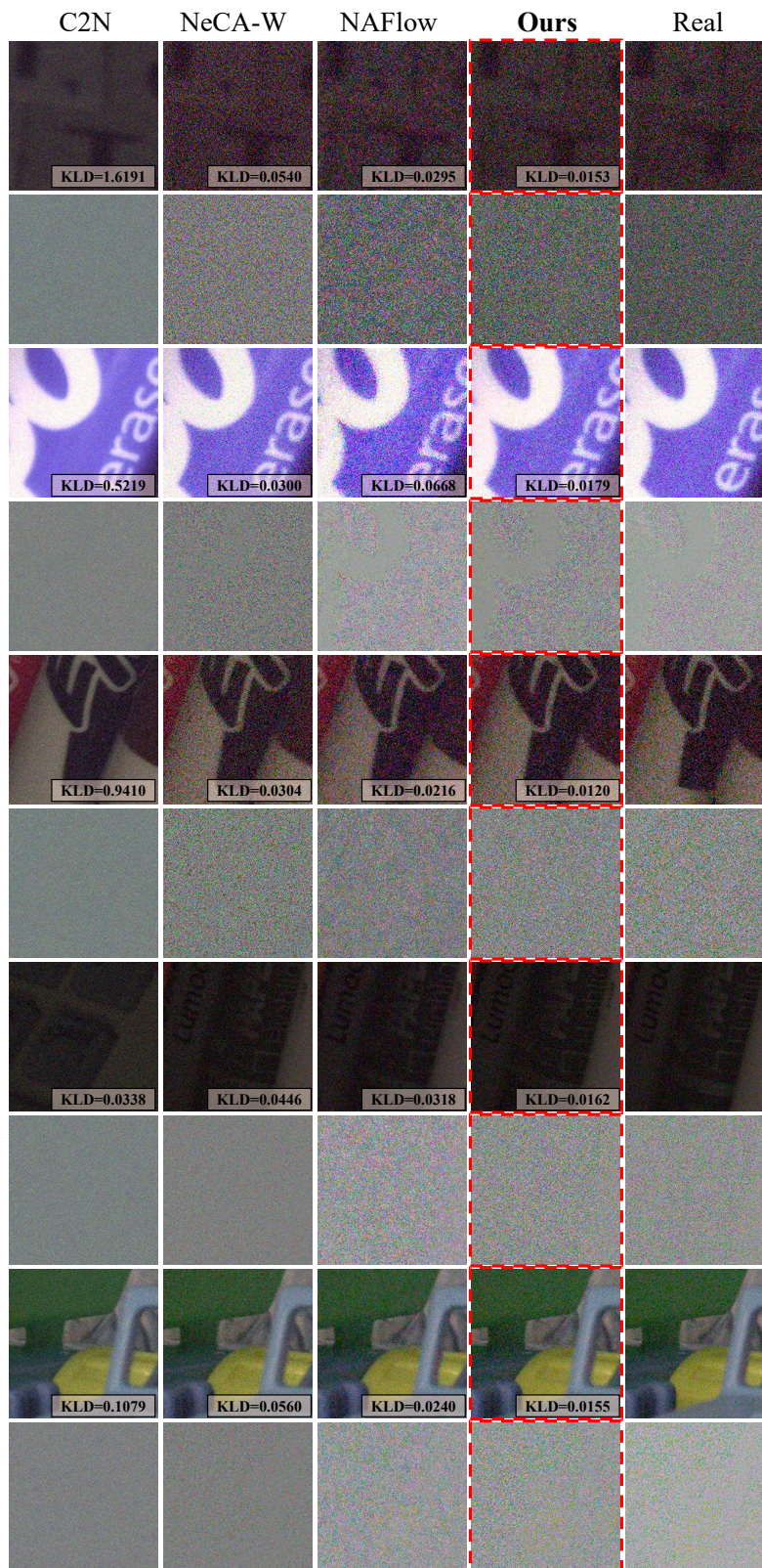


Figure S3. Visualization of synthetic noisy images on the SIDD validation set. From left to right: C2N, NeCA-W, NAFlow, Ours (PNG), and real noisy images.

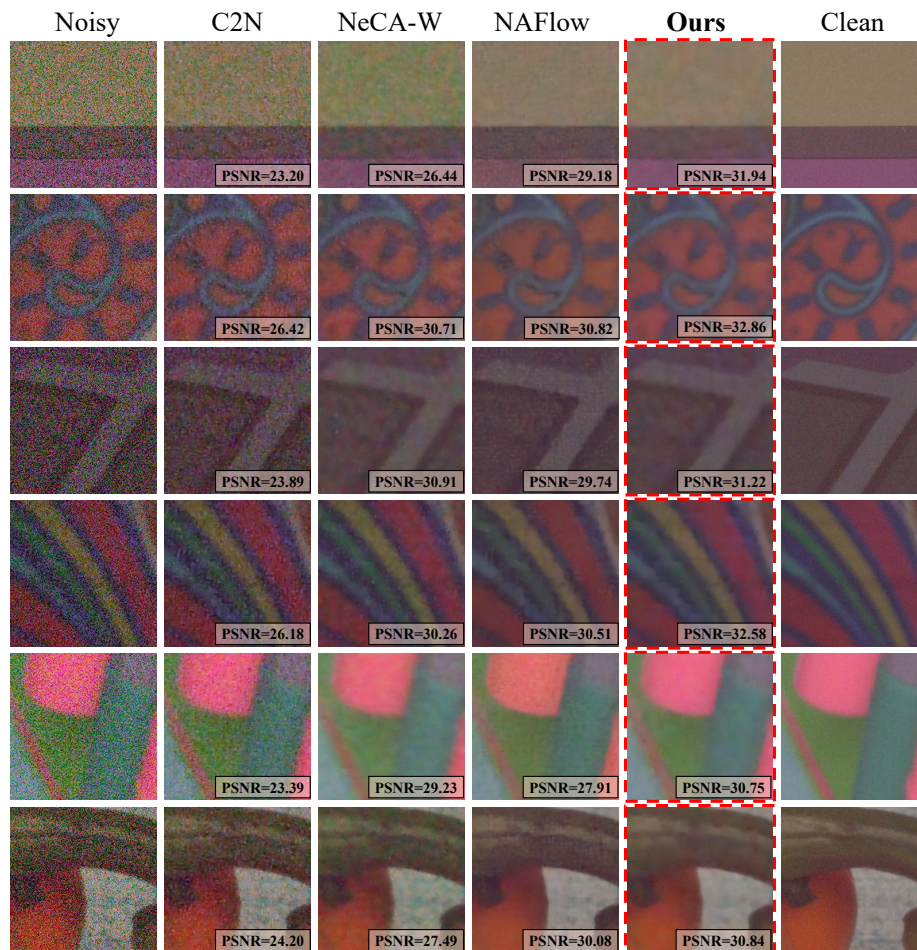


Figure S4. Visual comparison on denoising results with PSNR \uparrow on SIDD validation set from DnCNN trained on each method.